photonics

MDPI

Article

Goniopolarimetric Properties of Typical Satellite Material Surfaces: Intercomparison with Semi-Empirical pBRDF Modeled Results

Min Yang [1,*], Hongxia Mao [1], Jun Wu [2], Chong Zheng [1] and Li Wang [1]

[1] National Key Laboratory of Scattering and Radiation, Beijing 100854, China; 15101539272@163.com (H.M.); casic_zhengchong@126.com (C.Z.); wangli207@vip.sina.com (L.W.)
[2] Key Laboratory of General Optical Calibration and Characterization, Hefei Institutes of Physical Science, Chinese Academy of Sciences, Hefei 230031, China; wujun@aiofm.ac.cn
* Correspondence: yamor12@126.com

Abstract: Light reflected from satellite surfaces is polarized light, which plays a crucial role in space target identification and remote sensing. To deepen our understanding of the polarized reflectance property for satellite material surface, we present the experiments of polarimetric laboratory measurements from two typical satellite materials in the wavelength range of 400–1000 nm by using a goniometer instrument. The bidirectional polarized reflectance factor (BPRF) is used to describe the polarization characteristics of our samples. The polarized spectral reflectance and distribution of BPRF for our datasets are analyzed. Furthermore, five semi-empirical polarized bidirectional reflectance distribution functions (pBRDFs) models for polarized reflectance of typical satellite material surfaces (Preist–Germer model, Maxwell–Beard model, three-component model, Cook–Torrance model, and Kubelka–Munk model) are quantitatively intercompared using the measured BPRFs. The results suggest that the measured BPRFs of our samples are spectrally irrelevant, and the hemispherical distribution of BPRFs is obviously anisotropic. Except for the Preist–Germer model, the other semi-empirical models are in good agreement with the measured BPRF at the selected wavelengths, indicating that we can accurately simulate the polarized reflectance property of the satellite surface by using the existing polarimetric models. The Kubelka–Munk pBRDF model best fits the silver polyimide film and white coating surfaces with RMSE equal to 3.25% and 2.03%, and the correlation coefficient is 0.994 and 0.984, respectively. This study can be applied to provide an accurate pBRDF model for space object scene simulation and has great potential for polarization remote sensing.

Keywords: polarized bidirectional reflectance distribution function; bidirectional polarized reflectance factor; spectral polarization; satellite material

check for updates

Received: 11 November 2024
Revised: 18 December 2024
Accepted: 26 December 2024
Published: 27 December 2024

Citation: Yang, M.; Mao, H.; Wu, J.; Zheng, C.; Wang, L. Goniopolarimetric Properties of Typical Satellite Material Surfaces: Intercomparison with Semi-Empirical pBRDF Modeled Results. *Photonics* **2025**, *12*, 17. https://doi.org/10.3390/photonics12010017

1. Introduction

Light reflected from on-orbit satellite surfaces can be represented by polarization, which is mainly related to the information such as target surface shape, material properties, operational status, and observation geometry. By analyzing the results of optical polarization observation of satellites with different shapes, the United States Air Force [1] has demonstrated that polarization observation can be used to test the state of on-orbit targets and determine the influence of target materials and the space environment on the optical properties of targets. Pesses [2] developed a long-wave infrared spectropolarimetric signature model for space objects and simulated the intensity and polarization of a global positioning system satellite under different spinning and tumbling observation conditions. The simulations suggested that polarimetric observations could provide a more sensitive way to detect and identify space objects. Space object polarization signature modeling can simulate the polarization characteristics of an object at different orientations, and this information supports accurate space object detection or recognition [3].

Bidirectional reflectance distribution function (BRDF) was introduced by Nicodemus [4] and denotes a fundamental optical property of the material, representing the reflected energy distribution of an incident wave in a certain direction in a hemispheric space on the surface. BRDF is applied in many fields, including object optical signature modeling [5], optical remote sensing [6], object identification [7], and computer vision [8]. The polarization property of the satellite material surface can be described by pBRDF, which is derived from the BRDF. A method of quantifying the pBRDF is required to measure the pBRDF data of material surfaces by using an incident light and an observation system. In the ideal case, we should measure over the full hemispherical range of incident light and observation orientations. However, the measured data are very huge, making them challenging to measure [9,10]. Therefore, it is necessary to develop a precise pBRDF model to predict the pBRDF values under arbitrary conditions.

The popular pBRDF model is the semi-empirical model, developed following the basic physical parameters and experimental data. In the literature, many pBRDF models of material surfaces have been proposed. Priest and Germer [11,12] derived a pBRDF model by combining the Fresnel reflection and Snell's law [13] in the microfacet model, and the model can describe the highly absorbing and reflective rough surfaces. In 2009, Hyde et al. [14] developed a novel pBRDF model for dielectric and metallic surfaces. This model incorporates an ideal Lambertian diffuse scattering component and a shadowing term. Diner et al. [15] presented a pBRDF model using the polarization imaging observation data, which consists of a volume component and a specular reflection component generated by the microfacet model. Zhan et al. [16] developed a modified pBRDF model with a volume scattering component based on the Kubelka–Munk theories [17,18] and estimated the refractive index of the material surface using this model. Zhu [3] proposed a pBRDF model with the basis of a three-component assumption and applied it to analyze the polarization property of the coating surfaces. These semi-empirical pBRDF models cited above are only focused on the degree of linear polarization (DoLP) [10,16], Stokes parameters [15], and Muller matrix [3,11,12] property of rough material surface, while none of them use the BPRF generated from the Stokes parameters, usually described to the natural surfaces [19–21], to represent the inherent polarization reflectance characteristics of satellite material.

Despite some of these models being compared over a class of material, an intercomparison of all these semi-empirical models over satellite material has not been conducted. In the field of space object polarization signature modeling, there is no clear consensus on the most available pBRDF models to use for a given satellite surface. The relative strengths and weaknesses of the various pBRDF models are not always evident. Additionally, there have been no studies comparing the existing pBRDF models with the measured polarization data and presenting the optimal fitness parameters of models for satellite material surfaces. Combining the measured results with pBRDF models is valuable for representation of the inherent polarization characteristics of satellite material surfaces. Therefore, the purpose of this paper is to quantitatively intercompare typical pBRDF models using the BPRF data of different satellite material surfaces, trying to obtain which model is most suitable for predication of the BPRF of the satellite material surfaces, thereby providing an accurate pBRDF model for space object simulation and real scene rendering.

In this study, the measured method of BPRF and the introduction of the existing pBRDF models are given in Section 2. The measurement system and samples are shown in Section 3. The spectral property and distribution characteristics of BPRF have been analyzed based on the measured results in Section 4. The results of the comparison of these pBRDF models are presented in Section 5. Sections 6 and 7 provide discussion and conclusions, respectively.

2. Theory

2.1. Definition of Polarization Light

Stokes vector [22] can describe the polarized state of light, $S = [I, Q, U, V]^{\mathrm{T}}$, as shown in the following:

$$\begin{cases} I = \frac{2}{3}[I(0^\circ) + I(60^\circ) + I(120^\circ)] \\ Q = \frac{2}{3}[2I(0^\circ) - I(60^\circ) - I(120^\circ)] \\ U = \frac{2\sqrt{3}}{3}[I(60^\circ) - I(120^\circ)] \\ V = I_r - I_l \end{cases} \tag{1}$$

where $I(\theta)$ (θ = 0°, 60°, 120°) denotes the measured polarization intensity with the polarized analyzer at 0°, 60°, and 120°. I denotes the total radiance intensity, Q refers to the difference between parallel and perpendicular polarization, U denotes the degree of the diagonal polarizing component in the 45° direction. V is the circular polarization, which is usually neglected [23].

The *BPRF* is used to characterize the polarized reflectance radiance generated from the object surface. The definition of BPRF is the ratio between the polarized reflected radiation on the object surface and the incident irradiance under the same incident and detection conditions. It is written as follows:

$$BPRF(\theta_i, \phi_i, \theta_r, \phi_r) = \frac{\pi\sqrt{Q^2 + U^2}}{E\cos\theta_i} \tag{2}$$

where θ_i and ϕ_i are the incident zenith and azimuth angle, respectively. θ_r and ϕ_r are the viewing zenith and azimuth angle, respectively. E is the total incident irradiance. The incident irradiance can be obtained by measuring the radiance of an ideal Lambertian standard surface with the known hemispherical direction reflectance. The expression is written by the following:

$$E\cos\theta_i = \frac{\pi L_{ref}}{\rho} \tag{3}$$

where L_{ref} is the radiance of Lambertian standard. ρ is the hemispherical direction reflectance. Then, combining with the Equation (2), the *BPRF* is written by the following:

$$BPRF(\theta_i, \phi_i, \theta_r, \phi_r) = \frac{\sqrt{Q^2 + U^2}}{L_{ref}}\rho \tag{4}$$

We also measure the bidirectional reflectance factor (*BRF*) [24] and DoLP of our samples. The BRF is defined as a ratio of radiant flux (dL_{sample}) reflected by a sample surface in a particular direction to the reflected radiant flux (dL_{ref}) from an ideal Lambertian standard surface, and can be written as follows:

$$BRF(\theta_i, \phi_i, \theta_r, \phi_r) = \frac{dL_{sample}}{dL_{ref}}\rho \tag{5}$$

The *DoLP* [25] represents the proportion of linear polarized reflectance of the target to the total reflectance. The expression can be given as follows:

$$DoLP = \frac{\sqrt{Q^2 + U^2}}{I} \tag{6}$$

2.2. Existing Semi-Empirical pBRDF Models

In this paper, five semi-empirical pBRDF models, Preist–Germer model, Maxwell–Beard model [25], three-component model, Cook–Torrance model [26,27], and Kubelka–Munk model [28], are used to simulate the BPRF of satellite material surface. Then, we quantitatively intercompare these modeled results and measured BPRF values.

(1) Preist–Germer model

The pBRDF model was developed for rough surfaces based on the microfacet theory. The model follows:

$$R_p = \frac{1}{2\pi}\frac{1}{4\sigma^2}\frac{1}{\cos^4\alpha}\frac{\exp\left(-\frac{\tan^2\alpha}{2\sigma^2}\right)}{\cos\theta_i\cos\theta_r}\boldsymbol{M}(\theta_i,\theta_r,\Delta\phi) \tag{7}$$

$$\cos\alpha = (\cos\theta_i + \cos\theta_r)/(2\cos\beta) \tag{8}$$

$$\cos(2\beta) = \cos\theta_i\cos\theta_r + \sin\theta_i\sin\theta_r\cos\Delta\phi \tag{9}$$

where α is the angle between the normal direction of the mean surface and micro-surface. β is the polar angle of the microfacet. σ is the slope variance of microfacet. $\boldsymbol{M}$ is the Fresnel reflectance Muller matrix constructed by Jones matrix components [12]. $\Delta\phi = \phi_r - \phi_i$ denotes the relative azimuth angle.

(2) Maxwell–Beard model

The Maxwell–Beard model is shown as follows:

$$R_p = f_{spec}(\theta_i,\theta_r,\Delta\phi) + f_{vol}(\theta_i,\theta_r,\Delta\phi) = \frac{\boldsymbol{R}_F(\beta)}{4\cos\theta_i\cos\theta_r}p(\alpha)S_{MB} + f_{vol}^{MB}(\theta_i,\theta_r,\Delta\phi) \tag{10}$$

$$f_{vol}^{MB} = \left(k_{dif} + \frac{2k_{vol}}{\cos\theta_i + \cos\theta_r}\right)\boldsymbol{M}^{vol} = \left(k_{dif} + \frac{2k_{vol}}{\cos\theta_i + \cos\theta_r}\right)\begin{bmatrix}1&0&0&0\\0&0&0&0\\0&0&0&0\\0&0&0&0\end{bmatrix} \tag{11}$$

$$S_{MB} = \frac{1 + \frac{\alpha}{\Omega}\exp\left(-\frac{2\beta}{\tau}\right)}{1 + \frac{\alpha}{\Omega}} \tag{12}$$

$$p(\alpha) = \frac{B\exp\left(-\frac{\tan^2\alpha}{2\sigma^2}\right)}{2\pi\sigma^2\cos^3\alpha} \tag{13}$$

where $\boldsymbol{R}_F(\beta)$ is also the Fresnel reflectance Muller matrix. k_{dif} and k_{vol} are the diffuse component and volumetric scattering parameters, respectively. $\boldsymbol{M}^{vol}$ is the depolarization matrix. B, τ, Ω are the fit parameters. $p(\alpha)$ is the probability distribution function. S_{MB} is a shadowing term.

(3) Three-component model

The three-component model for satellite coatings has been developed based on fundamental principles of the specular reflection, the multiple reflection, and volume scattering. The model can be expressed as follows:

$$R_p = k_s f_s + k_m f_m + k_v f_v \tag{14}$$

$$f_s = \frac{1}{2\pi}\frac{1}{4\sigma^2}\frac{1}{\cos^4\alpha}\frac{\exp\left(-\frac{\tan^2\alpha}{2\sigma^2}\right)}{\cos\theta_r\cos\theta_i}G\boldsymbol{M}(\theta_i,\theta_r,\Delta\phi) \tag{15}$$

$$f_m = \cos^N\theta_r\boldsymbol{M}^m \tag{16}$$

$$f_v = 1 \cdot \boldsymbol{M}^v \tag{17}$$

Here, k_s, k_m, and k_v are the coefficients. G is the shadowing term given by Blinn [29]. N is a measurable parameter related to the illuminated surface. $\boldsymbol{M}^m$ and $\boldsymbol{M}^v$ are also the depolarization matrices.

(4) Cook–Torrance model

Cook and Torrance [26,27] established a pBRDF model for material surfaces based on the microfacet theory. The model is followed by a sum of a polarizing reflection term and a depolarizing volumetric scattering term. It is written as follows:

$$R_p = f_{microfacet}(\theta_i, \theta_r, \Delta\phi) + f_{vol}(\theta_i, \theta_r, \Delta\phi) \tag{18}$$

$$f_{microfacet} = k_c \frac{\exp\left(-\frac{\tan^2\alpha}{\sigma^2}\right) G(\theta_i, \theta_r, \Delta\phi)}{\pi\sigma^2 \cos\theta_{\mathrm{i}} \cos\theta_r \cos^4\alpha} \boldsymbol{M}(\theta_i, \theta_r, \Delta\phi) \tag{19}$$

$$f_{vol} = \frac{k_d}{\pi} \boldsymbol{D} \tag{20}$$

Here, k_c and k_d are the fit parameters. $\boldsymbol{D}$ is the depolarization matrix.

(5) Kubelka–Munk model

Yang et al. [28] proposed a modified microfacet model for material surface, incorporating both specular reflection and diffuse scattering. This model is based on the integration of microfacet theory and Kubelka–Munk theory. The expression is provided by the following:

$$R_p = \zeta \frac{G(\theta_i, \theta_r, \Delta\phi)}{8\pi\sigma^2 \cos^4\alpha} \frac{\exp\left(-\frac{\tan^2\alpha}{2\sigma^2}\right)}{\cos\theta_i \cos\theta_r} \boldsymbol{M}(\theta_i, \theta_r, \Delta\phi) + \frac{\cos\theta_r}{\pi} \frac{(1-R_i)(1-R_b)}{1-R_b R_\infty} \boldsymbol{M}^{vol} \tag{21}$$

where ζ is a scaling parameter. R_i represents the Fresnel reflection of light incident from air to a material surface. R_b denotes the Fresnel reflectance of diffuse light that traverses the material and the thin layer–air interface on the material surface [13]. R_∞ signifies the relative diffuse reflection coefficient for an infinite thickness of the material. This coefficient can be treated as a fitting parameter.

3. Measurement System and Samples

To compare the five existing pBRDF models, we perform the BPRF measurements for two typical of the thermal control materials on satellite surfaces: silver polyimide film and white coating, as shown in Figure 1. The silver polyimide film (Figure 1a) is cladding materials for the satellite's surface with varying degrees of undulating surface states that generate different polarized reflectance properties when exposed to sunlight. The white coating material (Figure 1b) is created by spraying white paint on metallic aluminum and has a rough and flatter surface.

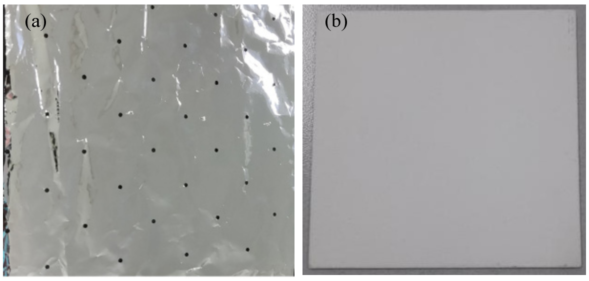

Figure 1. The picture of typical satellite material: (**a**) silver polyimide film, and (**b**) white coating.

The Northeast Normal University Laboratory Goniospectrometer System [30] is designed to perform spectral BPRF measurements. The basic measuring instrument consists of an incident light source, a goniometer, and a spectroradiometer. The incident source is a 100 W tungsten halogen lamp, and produces the non-polarized parallel light. The goniometer is 1.2 m. The azimuth and zenith direction of the goniometer can be changed 0°~360° and 0°~90° using a stepping motor, respectively. The spectroradiometer has an effective wavelength range of 350–2500 nm, which is mounted on a rotating half-circle arc that can be titled up to 90° from the zenith. The field of view is 8°. A polarizer is installed in front of the optical fiber of the spectroradiometer, and it allows free rotation from 0° to 360° to achieve the measurement of the polarization characteristics. The polarizer and the optical fiber probe of the spectroradiometer are mounted on the goniometer, enabling movement at any point on the hemisphere above a sample.

Figure 2a shows the measurement schematic diagram. The BPRF measurement is carried out in laboratory conditions with the incident zenith angles at 30°, 40°, 50°, and 60° in the wavelength of 400–1000 nm. When the incident zenith angle is fixed, the viewing zenith angle is started at 0°, and changes to 60° at intervals of 10° (0°, 10°, 20°, 30°, 40°, 50°, and 60°) at all azimuth angles. The azimuth angle changes from 0° to 360° with the interval of 30° (0°, 30°, 60°, 90°, 120°, 150°, and 180°). During the measurement, we assume the polarization distribution of the sample is left–right symmetrical based on the principal plane ($\Delta\phi = 0°$ and $\Delta\phi = 180°$). Due to the limitations of the instrument in the backward scattering direction, the incidence equal to the viewing zenith angle position at 0° azimuth angle could not be measured. A total of 42 measurement positions are investigated for each sample with one incident zenith angle, as shown in Figure 2b. The black points represent the viewing zenith positions. The incident zenith angle is 40°. To fill the gap of the polar plot, we replaced the BPRF value by the mean value of the two adjacent viewing zenith angles (e.g., the measured BPRF at viewing angle of 40° is replaced by the mean value at the viewing zenith angles of 30° and 50° in the backward direction in the principle plane) at the relative azimuth angle of 0°. A Spectralon panel is employed as an ideal Lambertian standard surface exhibiting a hemispherical directional spectral reflectance approaching 1. The BPRF, BRF, and DoLP were solved using Equations (4), (5) and (6), respectively.

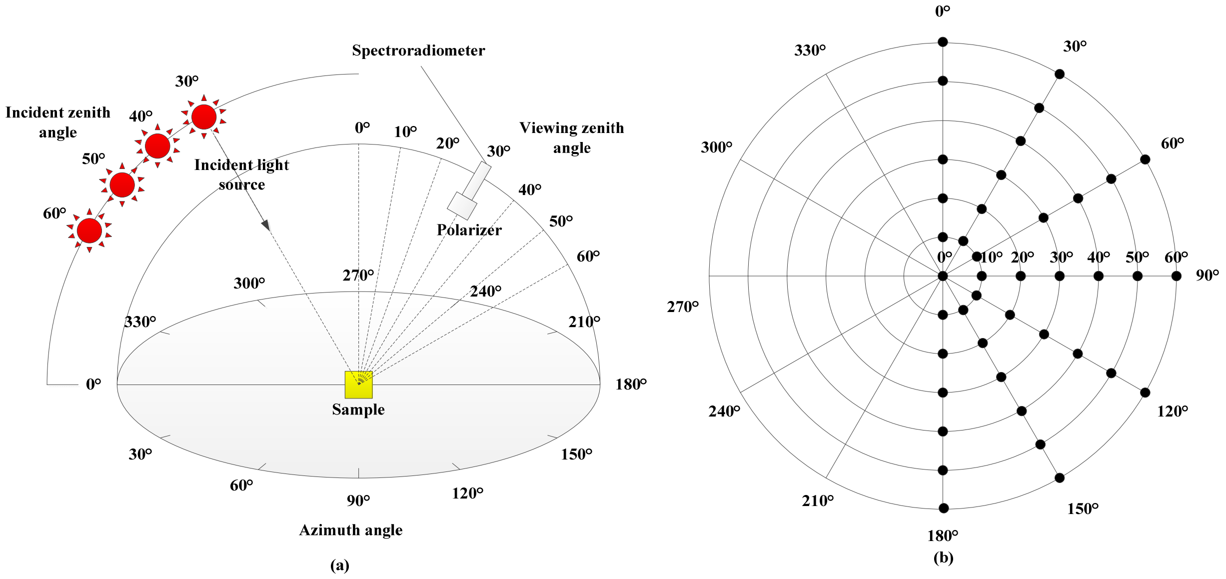

Figure 2. (**a**) The schematic diagram of measurement. (**b**) The grid is the hemispherical sampling pattern when the incident zenith angle is 40°.

4. Results of Measurements

4.1. The Polarized Spectral of Typical Satellite Material Surfaces

In this section, we will verify the accuracy of our measured results for satellite material samples. Figure 3 illustrates the BRF curves of our samples at different viewing zenith angles in the principal plane, with the incident zenith angle of 40°. It can be found that the BRF varies gently with wavelength, and a BRF peak is observed at a viewing zenith angle of 40° for silver polyimide film. This phenomenon can be attributed to the relatively smooth surface structure or smaller roughness surface of the silver polyimide film, resulting in a reflectance peak when the viewing zenith angle is in close proximity to the incident zenith angle. For white coating, the maximum BRF that occurs at the viewing zenith angle is 50°, and is not in a small lobe in specular reflection ($\theta_i = \theta_r = 40°$). This is because the white coating has a rough surface structure, which can broaden the specular lobe and increase the diffuse scattering. The BRF increases gradually with a wavelength of 400–450 nm, and the BRF is essentially unchanged in a range of 500–1000 nm. The spectral BRF appears with few resonances at 450 nm and 550 nm. This is mainly due to the BRF being calculated from the total polarized reflected intensity [19], and the lower transmittance of the polarizer at lower wavelengths will result in a low signal-to-noise ratio in the measured data. The measured results for silver polyimide film and white coating are a common phenomenon for manmade objects [10,24,31].

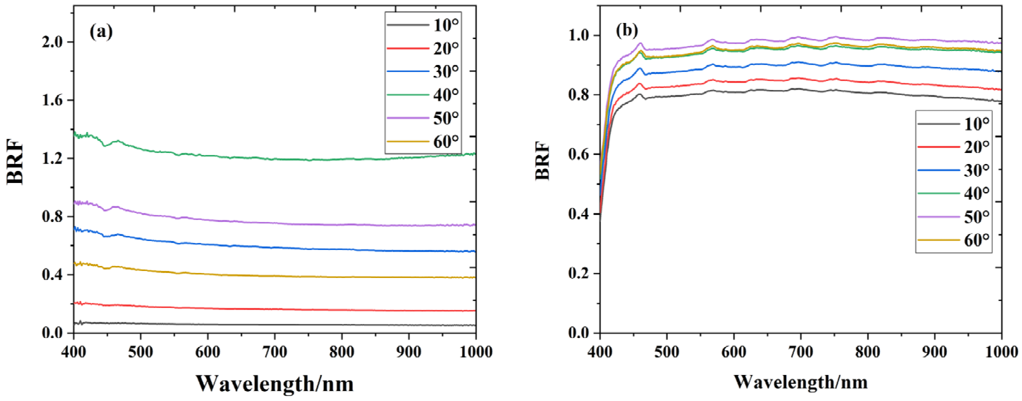

Figure 3. The BRF spectrum curves of the (**a**) silver polyimide film and (**b**) white coating at different viewing zenith angles ($\Delta\phi = 180°$) when the incident zenith angle is 40°.

To study the polarized properties of our samples, the DoLP was calculated for the silver polyimide film and white coating samples. Figure 4 illustrates the spectral DoLP of two samples at different viewing zenith angles in the principle plane, with the incident zenith angle of 40°. It can be seen that the spectral DoLP is inversely proportional to the spectral BRF for the same incident and viewing zenith angle. Moreover, the DoLP increases with an increase in the viewing zenith angle. This phenomenon can be explained by the Fresnel polarization reflection coefficient, which exhibits a positive correlation with both the incident zenith angle and the detection zenith angle (phase angle) in the case of a consistent target.

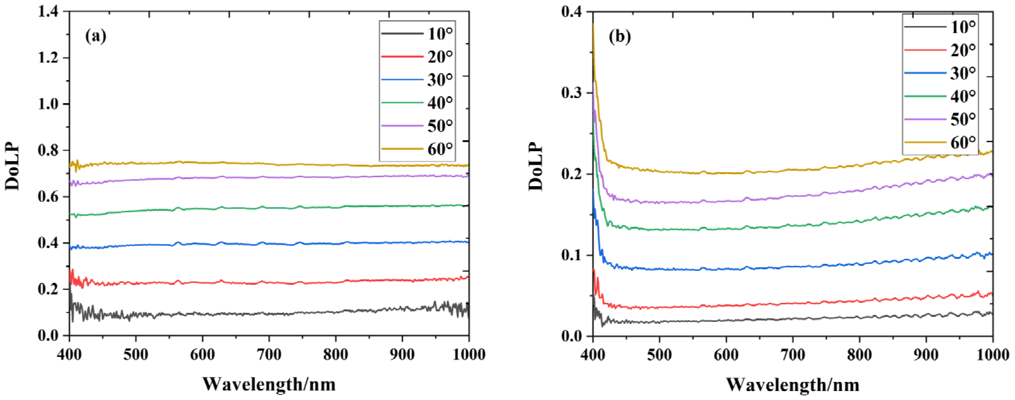

Figure 4. The DoLP curves of the (**a**) silver polyimide film and (**b**) white coating at different viewing zenith angles ($\Delta\phi$ = 180°) when the incident zenith angle is 40°.

Figure 5 shows the spectral BPRF of two samples at different viewing zenith angles in the principle plane, with the incident zenith angle of 40°. The BPRF is employed to quantify the degree of polarized reflectance exhibited by a target, which is widely acknowledged that the smoother the surface, or the lesser the roughness, the greater the value of the polarized reflectance ratio. As can be seen from the figure, the BPRF of the two samples shows the same change with the BRF. The BPRF causes a small variation in wavelength, which has the same spectral characteristics as the results observed for natural feature surfaces in previous studies [15,19–21]. However, the BPRF value of the satellite material is much greater than that of the natural surfaces, which is not reported in the other literature. The maximum BPRF value of the silver polyimide film is observed in the specular direction, while the maximum BPRF value of the white coating occurs at an angle slightly larger than the specular direction. This means that there is a relationship between the polarization reflectance and roughness of the target.

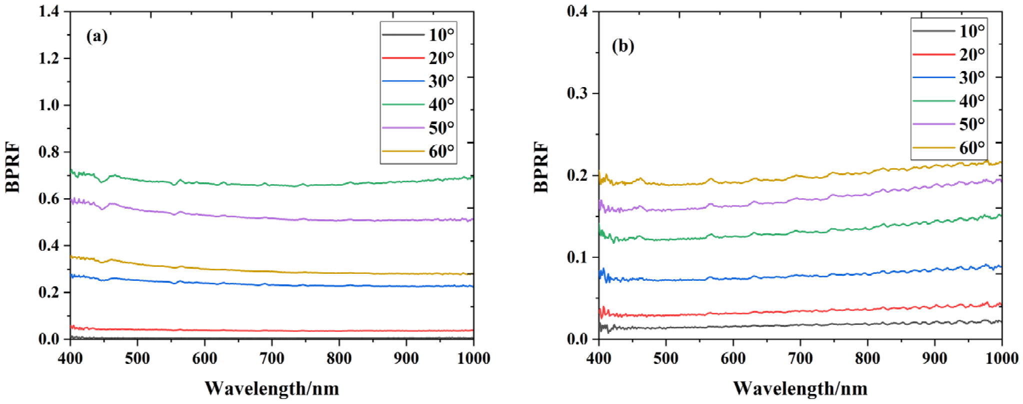

Figure 5. The BPRF curves of the (**a**) silver polyimide film and (**b**) white coating at different viewing zenith angles ($\Delta\phi$ = 180°) when the incident zenith angle is 40°.

4.2. The Distribution of Polarization for Typical Satellite Material Surfaces

To further study the distribution of the polarization reflectance of satellite material, we mainly show the BPRF of our samples at 560, 670, and 865 nm. We focused on these bands because these bands are common channels for satellite polarized remote sensing, which can obtain the multi-angle polarization information for target and natural surfaces. Figures 6 and 7 show the distribution of BPRF of satellite material samples at 560, 670, and 865 nm, with the incident zenith angle at 40°. The yellow dot means the position of incident zenith angle. It is clear that the BPRF of the silver polyimide film and white coating sample exhibits pronounced anisotropic, with the distribution of the BPRF at different wavelengths exhibiting minimal variation. This also suggests that the BPRF is wavelength-independent. The BPRF of the white coating increases with the increase of the viewing zenith angle in the forward scattering direction. In contrast, the silver polyimide film produced a peak when $\theta_i = \theta_r = 40°$.

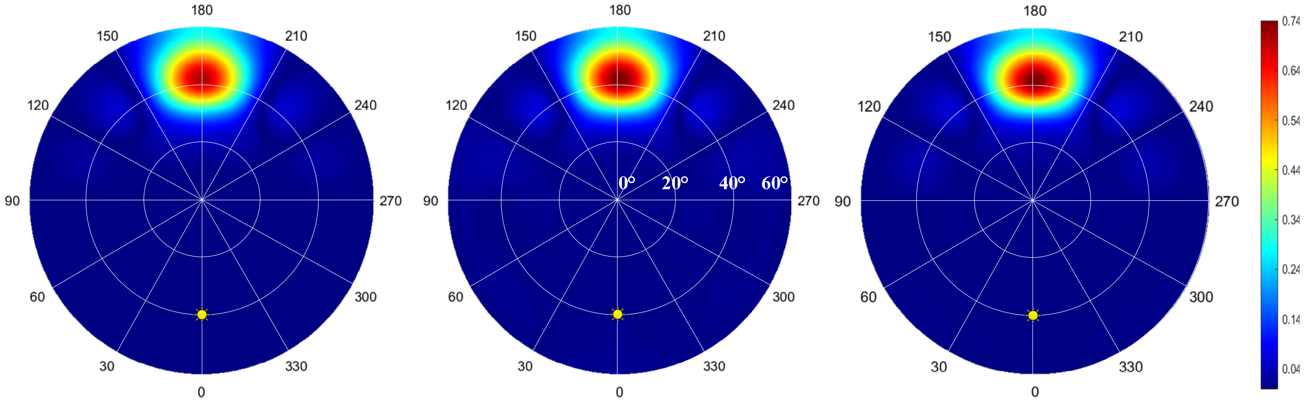

(a) 560nm **(b) 670nm** **(c) 865nm**

Figure 6. The hemisphere distribution of BPRF of the silver polyimide film at (**a**) 560 nm, (**b**) 670 nm, and (**c**) 865 nm, and the incident zenith angle is 40°.

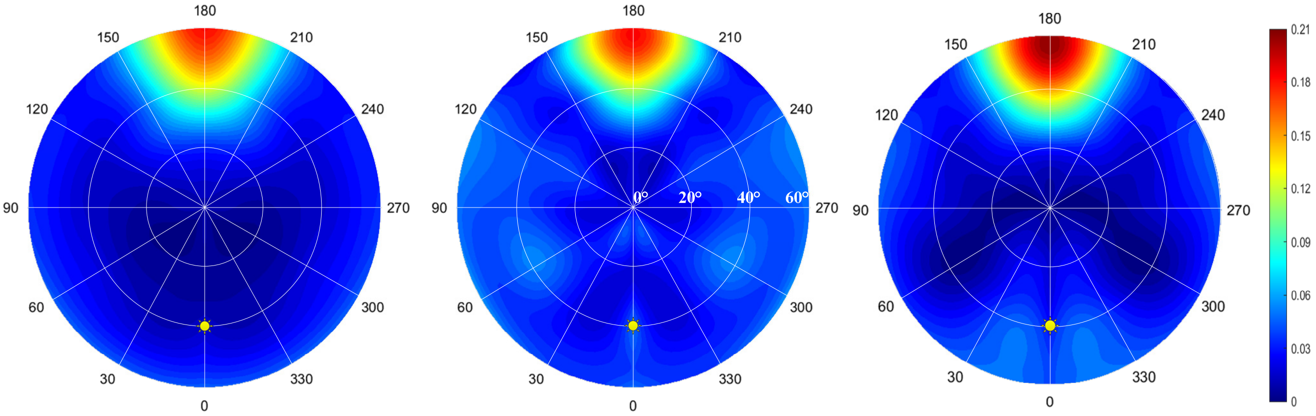

(a) 560nm **(b) 670nm** **(c) 865nm**

Figure 7. The hemisphere distribution of BPRF of the white coating at (**a**) 560 nm, (**b**) 670 nm, and (**c**) 865 nm, and the incident zenith angle is 40°.

To further verify the credibility of the measured data, we also show the distribution of the BPRF at the wavelength of 670 nm for incident zenith angles of 30°, 50°, and 60°, as seen in Figures 8 and 9. The yellow dot means the position of incident zenith angle. As the incident angle increases, the BPRF of silver polyimide film and white coating samples gradually increases. This phenomenon can be explained by the cosine law of incident light. The BPRF of the silver polyimide film, defined in Equation (4), is much greater than 1, which has not been noted by previous researchers. This is because the polarization mainly depends on the specular reflection, and the orientation and physical properties influence the distribution characteristics. The polarimetric measurements of our samples, which have the same distribution characteristics compared to those observed in previous studies [3,9,24,32,33], can be accurately applied to invert model parameters.

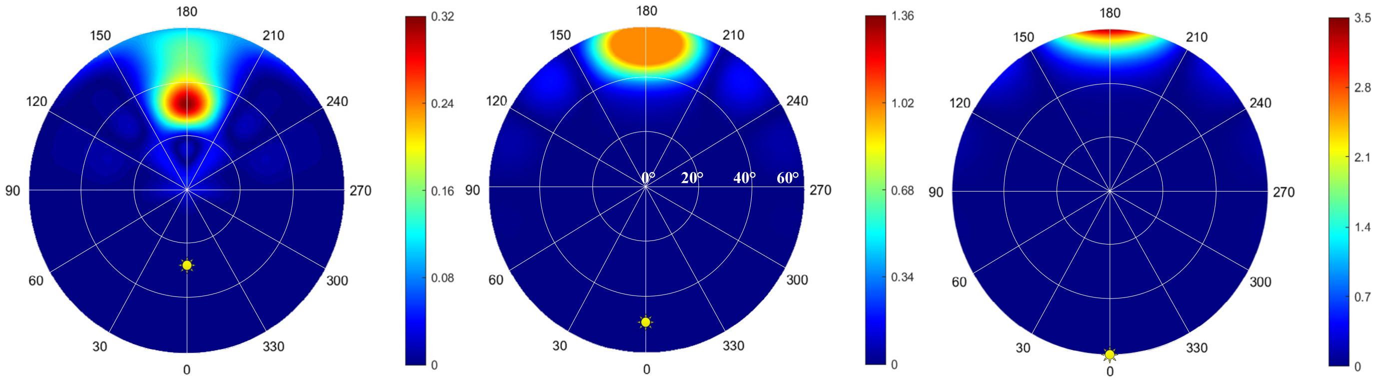

(a) 30° (b) 50° (c) 60°

Figure 8. The hemisphere distribution of BPRF of the silver polyimide film at 670 nm, and the incident zenith angles are (**a**) 30°, (**b**) 50°, and (**c**) 60°.

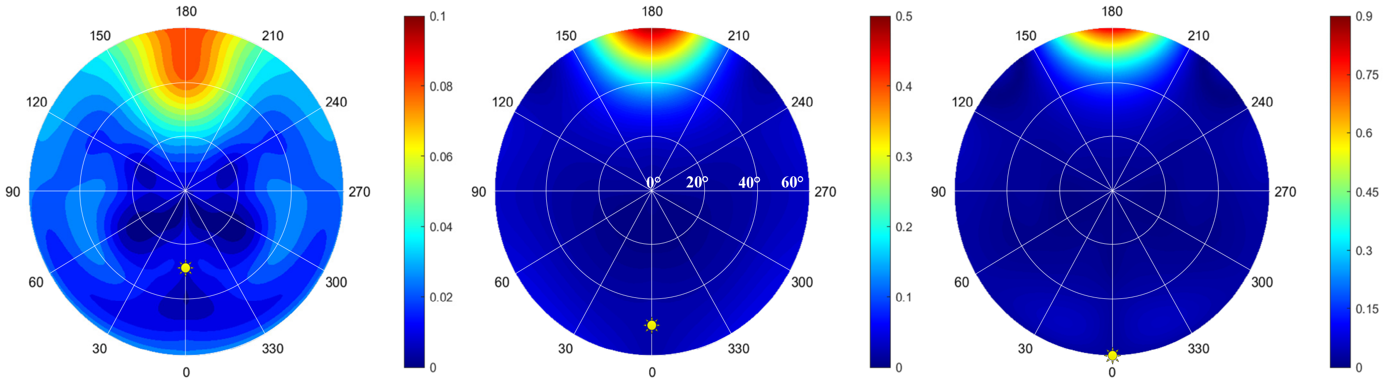

(a) 30° (b) 50° (c) 60°

Figure 9. The hemisphere distribution of BPRF of the white coating at 670 nm, and the incident zenith angles are (**a**) 30°, (**b**) 50°, and (**c**) 60°.

5. Intercomparison Between Measurements and Modeled Results

5.1. Model Parameters Determination

All of the existing semi-empirical pBRDF models contain several model parameters. The least squares fitting algorithm is applied to invert the model parameters. The root mean square error (*RMSE*) represents the deviation between the measured and simulated value. This can be given by the following:

$$RMSE = \sqrt{\frac{\sum_{i=1}^{N}\left(R_p^{mea} - R_p^{sim}\right)^2}{N}} \tag{22}$$

where R_p^{mea} and R_p^{sim} is measured and modeled value, respectively. N is the total number of measurements. All measured DoLPs for each satellite material sample at 560, 670, and 865 nm are used to fit the optimal model parameters. The measured BPRFs are then used to compare the modeled results based on these inverted parameters. Appendix A shows the best-fitting parameters of the five pBRDF models for silver polyimide film and white coating at selected wavelengths.

5.2. Intercomparison Between the Measured and Modeled Results

The BPRF is calculated from the inverted model parameters. The comparison of the simulated and the measured BPRF results for each satellite material sample in the hemispherical distribution at 865 nm and the incident zenith angle of 40° is shown in Figures 10 and 11. The yellow dot means the position of incident zenith angle. It can be seen that, with the exception of the Preist–Germer model, the other existing pBRDF models are in good agreement with most of the measured BPRF values. The measured and simulated BPRF at 865 nm have similar distribution characteristics. The Preist–Germer model disagrees well with the measurements of the silver polyimide film and the white coating (see Figures 10b and 11b). This is because the Preist–Germer model does not contain a diffuse reflection component and is only able to simulate materials with high specular reflection. It is not suitable for materials with high diffuse reflection. In addition, the Preist–Germer model has the lowest number of parameters, while the other models display a more significant number of parameters. This feature may enhance the model's adaptability. The reflection from the satellite material surface incorporates both specular and diffuse reflection, while the other models (Maxwell–Beard model, three-component model, Cook–Torrance model, and Kubelka–Munk model) include a diffuse component, thereby providing a better simulation of the polarized reflectance properties.

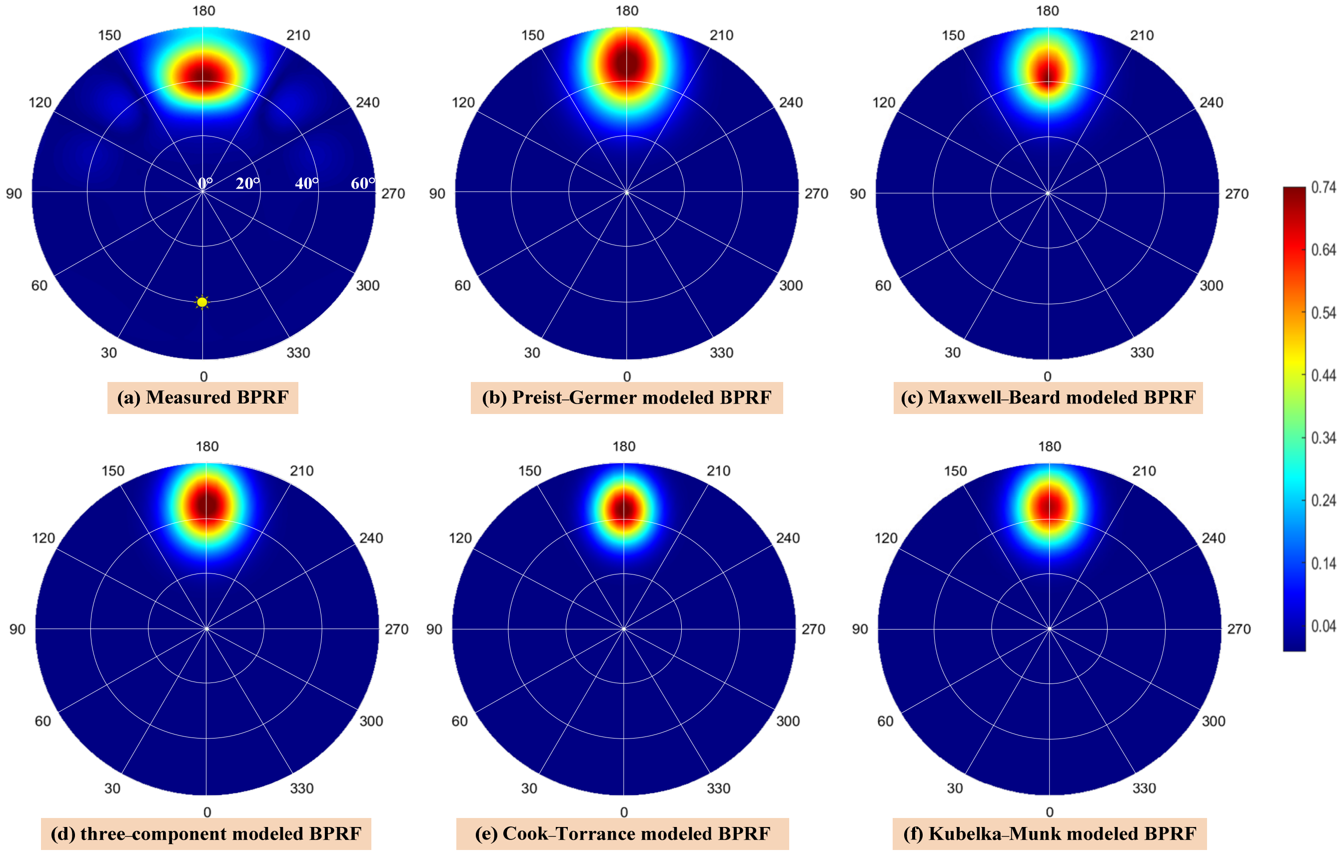

(a) Measured BPRF **(b) Preist–Germer modeled BPRF** **(c) Maxwell–Beard modeled BPRF**

(d) three-component modeled BPRF **(e) Cook–Torrance modeled BPRF** **(f) Kubelka–Munk modeled BPRF**

Figure 10. The hemisphere distribution of (**a**) the measured BPRF and (**b**–**f**) the modeled BPRF of the silver polyimide film at 865 nm, and the incident zenith angle is 40°.

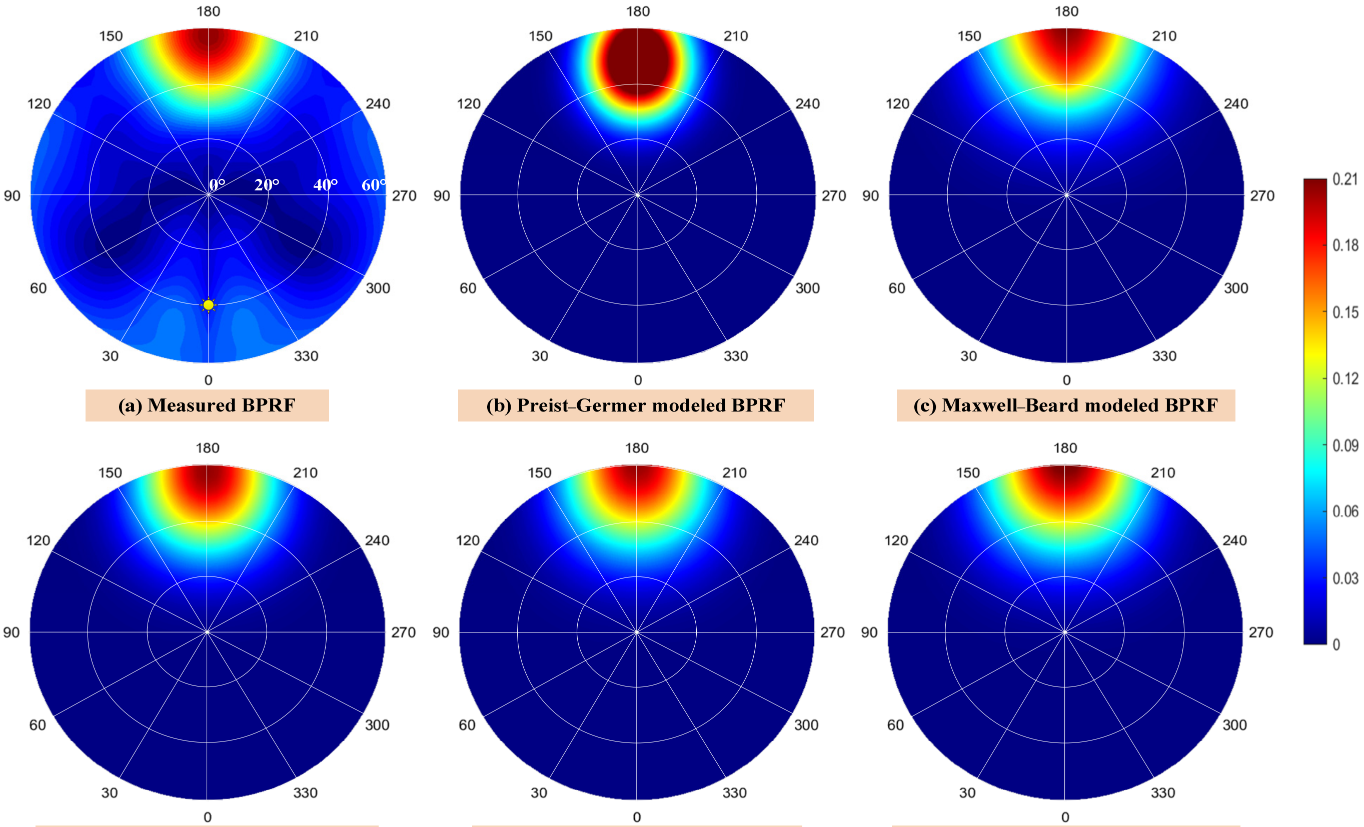

(a) Measured BPRF
(b) Preist–Germer modeled BPRF
(c) Maxwell–Beard modeled BPRF
(d) three-component modeled BPRF
(e) Cook–Torrance modeled BPRF
(f) Kubelka–Munk modeled BPRF

Figure 11. The hemisphere distribution of (**a**) the measured BPRF and (**b**–**f**) the modeled BPRF of the white coating at 865 nm, and the incident zenith angle is 40°.

Additionally, to further quantitatively compare the difference between the modeled and the measured results, we list the measured BPRFs against the best-fit models for silver polyimide film and white coating samples of 560, 670, and 865 nm over all measurement directions and incident zenith angles, as seen in Figure 12. The red scatter dots mean the difference between modeled and measured BPRF values. The RMSE and correlation coefficient (Cor) are used to judge the performance of the semi-empirical pBRDF model. The Cor [34] is used to describe the correlation between the measured and simulated results. Table 1 shows the fitting results of the five semi-empirical pBRDF models. Note that the Maxwell–Beard model, three-component model, Cook–Torrance model, and Kubelka–Munk model provide the best fitting of the BPRF with the largest RMSE of 0.0544 and the smallest correlation coefficient of 0.978. Compared to them, the Kubelka–Munk model is fairly in agreement with the measured BPRF for the silver polyimide film and white coating samples. The RMSE is 0.0325 and 0.0203, and the maximum correlation coefficient is 0.994 and 0.984, respectively. This is because the Kubelka–Munk model incorporates the diffuse scattering component by the Kubelka–Munk theory [4], which is able to describe the scattering and absorption of light within the bulk of a material. In summary, the existing BPRF model can accurately describe the polarization reflectance characteristics of satellite material.

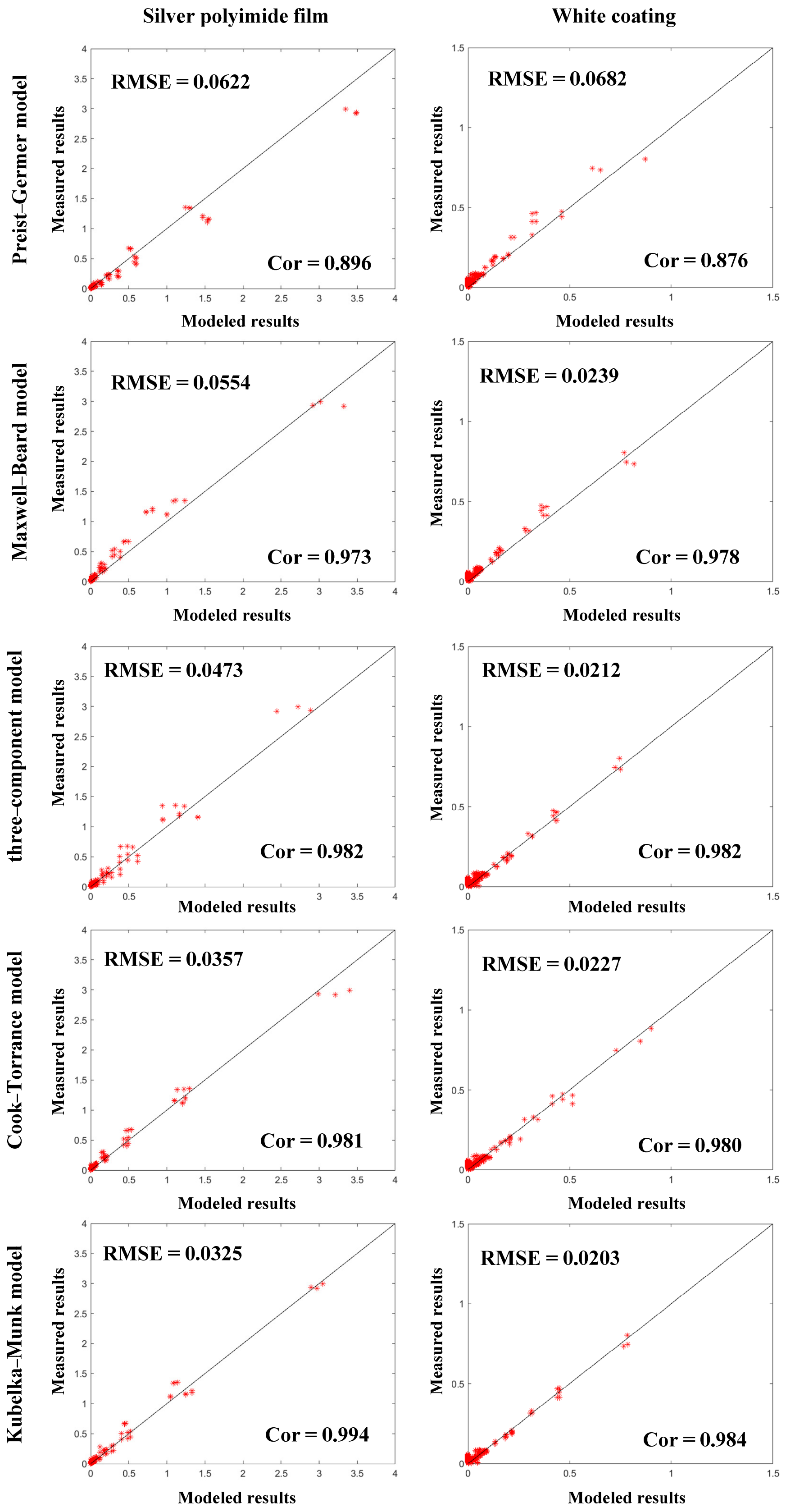

Figure 12. The comparison between measurements and modeled BPRF of our samples over all measured directions in all incident zenith angles.

Table 1. The fitting results of the five semi-empirical pBRDF models.

Samples	Index	Preist–Germer Model	Maxwell–Beard Model	Three–Component Model	Cook–Torrance Model	Kubelka–Munk Model
Silver polyimide film	RMSE	0.0622	0.0554	0.0473	0.0357	0.0325
	Cor	0.896	0.973	0.982	0.981	0.994
White coating	RMSE	0.0682	0.0239	0.0212	0.0227	0.0203
	Cor	0.876	0.978	0.982	0.980	0.984

6. Discussion

In this study, we have presented an experimental and semi-empirical pBRDF model intercomparison study of the satellite material surfaces. In general, the measured BRF, DoLP, and BPRF of the silver polyimide film and white coating are in accordance with the findings of previous studies [3,19]. A comparison of our experimental results with those of older studies reveals that the satellite material surface is capable of generating high BPRF, which differs from the vegetation [35]. Additionally, the Kubelka–Munk pBRDF model was also identified as the most accurate representation of the selected samples.

Regrettably, the comparative model analysis was limited to two types of materials: silver polyimide film (high reflectivity) and rough white coating (low reflectivity). We hope to add some studies on the polarization properties of new satellite materials in the future. Furthermore, surface roughness represents an important parameter for characterizing the surface condition of an object, and it is not quantified in this paper. The surface roughness of the samples could be measured using alternative approaches, thereby improving the inversion accuracy of pBRDF. The research results will be utilized to support polarization scene simulation.

7. Conclusions

This paper reports the polarized reflectance laboratory measurements from two typical satellite materials over different viewing directions and incident zenith angles in the range of 400–1000 nm. Our results confirmed that the BPRF for satellite material is spectrally irrelevant, and the distribution of BPRF is anisotropic. It is also worth noting that the maximum BPRF value is much greater than 1 for silver polyimide film, which has a smooth surface. This discrepancy has not been previously reported. The representative BPRFs generated from measurements of the silver polyimide film and white coating are used in the inversion of the model parameters of five semi-empirical pBRDF models and quantitatively compared. As expected, with the exception of the Preist–Germer model, the other existing pBRDF models are in good agreement with the measured results. Statistics also suggest the Kubelka–Munk model provides the best fitting of surface polarized reflectance for satellite material. The RMSE is 0.0325 and 0.0203, and the maximum correlation coefficient is 0.994 and 0.984 for silver polyimide film and white coating, respectively. The results indicate that we can accurately simulate the polarized reflectance property of satellite surfaces by using the pBRDF polarimetric models in visible and near-infrared bands. This study can be applied to research of satellite polarization characteristics, and may also possess great potential for space object polarization modeling.

Author Contributions: Methodology, M.Y.; software, J.W.; algorithm, C.Z.; validation, H.M. and L.W.; writing—review and editing, M.Y.; writing—review and editing, C.Z. All authors have read and agreed to the published version of the manuscript.

Funding: This research received no external funding.

Institutional Review Board Statement: No applicable.

Informed Consent Statement: No applicable.

Data Availability Statement: The original contributions are presented in this article; future inquires can be directed to the corresponding author.

Conflicts of Interest: The authors declare no conflicts of interest.

Appendix A

The optimal model parameters are shown as follows.

1. The Preist–Germer model parameters

Table A1. The optimal fitting parameters of the Preist–Germer model for silver polyimide film and white coating.

Wavelengths	Silver Polyimide Film				White Coating			
	n	k	σ	$RMSE$	n	k	σ	$RMSE$
560 nm	1.527	3.19×10^{-5}	0.105	0.110	1.221	7.17×10^{-7}	0.158	0.068
670 nm	1.451	1.26×10^{-8}	0.106	0.112	1.217	2.02×10^{-3}	0.161	0.068
865 nm	1.643	9.31×10^{-5}	0.105	0.108	1.207	0.181	0.163	0.069

2. The Maxwell–Beard model parameters

Table A2. The optimal fitting parameters of the Maxwell–Beard model for silver polyimide film and white coating.

Samples	Wavelengths	σ	τ	Ω	k_{dif}	k_{vol}	B	$RMSE$
Silver polyimide film	560	0.108	0.118	0.133	0.018	1.49×10^{-5}	1.000	0.043
	670	0.109	0.007	0.109	0.015	2.65×10^{-14}	0.949	0.048
	865	0.106	0.161	0.186	0.006	0.005	0.996	0.050
White coating	560	0.197	0.223	0.486	0.140	3.22×10^{-9}	0.996	0.008
	670	0.198	0.317	0.485	0.166	1.74×10^{-7}	1.000	0.007
	865	0.196	0.479	0.462	0.194	4.98×10^{-6}	1.000	0.008

3. Three-component model parameters

Table A3. The optimal fitting parameters of the three-component model for silver polyimide film and white coating.

	Wavelengths	k_s	k_m	k_v	σ	$RMSE$
Silver polyimide film	560	0.366	1.677	−0.951	0.095	0.053
	670	0.386	0.050	−0.033	0.110	0.129
	865	0.374	0.981	2.622	0.088	0.055
White coating	560	0.225	4.76×10^{-5}	4.26×10^{-5}	0.173	0.011
	670	0.212	0.877	3.127	0.174	0.010
	865	0.183	9.24×10^{-8}	2.89×10^{-8}	0.170	0.023

4. The Cook–Torrance model parameters

Table A4. The optimal fitting parameters of the Cook–Torrance model for silver polyimide film and white coating.

Wavelengths	Silver Polyimide Film				White Coating			
	k_c	k_d	σ	$RMSE$	k_c	k_d	σ	$RMSE$
560 nm	0.179	0.121	0.118	0.045	0.582	0.159	0.269	0.011
670 nm	0.180	0.113	0.119	0.051	0.593	0.139	0.270	0.010
865 nm	0.231	0.128	0.121	0.056	0.570	0.115	0.231	0.011

5. The Kubelka–Munk model parameters

Table A5. The optimal fitting parameters of the Kubelka–Munk model for silver polyimide film and white coating.

Wavelengths	Silver Polyimide Film				White Coating			
	ζ	σ	R_d	$RMSE$	ζ	σ	R_d	$RMSE$
560 nm	0.762	0.103	0.202	0.035	0.210	0.179	0.087	0.016
670 nm	0.754	0.102	0.211	0.041	0.212	0.178	0.109	0.016
865 nm	0.531	0.082	0.206	0.050	0.208	0.177	0.232	0.017

References

1. Stead, R.P. *An Investigation of Polarization Produced by Space Objects*; Air Force Institute of Technology: Dayton, OH, USA, 1967.
2. Pesses, M.; Tan, J.; Hash, R.; Swartz, R. Simulation of LWIR polarimetric observations of space objects. In Proceedings of the Applied Imagery Pattern Recognition Workshop, 2002. Proceedings., Washington, DC, USA, 16–18 October 2002; pp. 164–170.
3. Liu, H.; Zhu, J.; Wang, K.; Xu, R. Polarized BRDF for coatings based on three-component assumption. *Opt. Commun.* **2017**, *384*, 118–124. [CrossRef]
4. Nicodemus, F. Directional reflectance and emissivity of an opaque surface. *Appl. Opt.* **1967**, *4*, 767. [CrossRef]
5. Willison, A.; Bedard, D. A novel approach to modeling spacecraft spectral reflectance. *Adv. Space Res.* **2016**, *58*, 1318–1330. [CrossRef]
6. Roujean, J.; Leroy, M.; Deschamps, P. A bidirectional reflectance model of the Earth's surface for the correction of remote sensing data. *J. Geophys. Res.* **1992**, *97*, 20455. [CrossRef]
7. Jiang, C.X.; Tan, Y.; Qu, G.N.; Lv, Z.; Gu, N.W.; Lu, W.J.; Zhou, J.W.; Li, Z.W.; Xu, R.; Wang, K.L.; et al. Super diffraction limitspectral imaging detection and material type identification of distant space objects. *Opt. Express* **2022**, *30*, 46911–46925. [CrossRef]
8. Westin, S.; Li, H.; Torrance, K. A comparison of four BRDF models. In Proceedings of the Eurographics Symposium on Rendering, Norköping, Sweden, 21–23 June 2004; pp. 1–10.
9. Yang, M.; Xu, W.; Li, J.; Zhou, Z. A modified version of BRDF model based Kubelka-Munk theory for coating materials. *Optik* **2019**, *193*, 162982. [CrossRef]
10. Sun, Z.; Wu, D.; Lv, Y. Photopolarimetric properties of a manmade target over a wide range of measurement directions. *Opt. Express* **2017**, *25*, A85–A100. [CrossRef]
11. Priest, R.; Germer, T. Polarimetric BRDF in the microfacet model: Theory and measurements. In Proceedings of the 2000 Meeting of the Military Sensing Symposia Specialty Sensors Group on Passive Sensors, Ann Arbor, MI, USA, 21–23 March 2000; Volume 1, pp. 169–181.
12. Priest, R.; Meier, S. Polarimetric microfacet scattering theory with applications to absorptive and reflective surfaces. *Opt. Eng.* **2002**, *41*, 988–993. [CrossRef]
13. Torrance, K.; Sparrow, E. Theory of off-specular reflection from roughened surfaces. *J. Opt. Soc. Am.* **1967**, *57*, 1105–1114. [CrossRef]
14. Hyde, M.; Schmidt, J.; Havrilla, M. A geometrical optics polarimetric bidirectional reflectance distribution function for dielectric and metallic surfaces. *Opt. Express* **2009**, *17*, 22138–22153. [CrossRef]
15. Diner, J.; Xu, F.; Martonchik, J.; Rheingans, B.; Geier, S.; Jovanovic, V.; Davis, A.; Chipman, R.; McClain, S. Exploration of a polarized surface bidirectional reflectance model using the ground-based multiangle spectropolarimetric imager. *Atmosphere* **2012**, *3*, 591–619. [CrossRef]

16. Zhan, H.; Voelz, D. Modified polarimetric bidirectional reflectance distribution function with diffuse scattering: Surface parameter estimation. *Opt. Eng.* **2016**, *55*, 123103. [CrossRef]
17. Kubelka, P. New contributions to the optics intensely light scattering materials, Part 1. *J. Opt. Soc. Am.* **1948**, *38*, 448–457. [CrossRef] [PubMed]
18. Murphy, A. Modified Kubelka-Munk model for calculation of the reflectance of coatings with optically-rough surfaces. *J. Phys. D Appl. Phys.* **2006**, *39*, 3571–3581. [CrossRef]
19. Sun, Z.; Peng, Z.; Wu, D.; Lv, F. Photopolarimetric properties of leaf and vegetation covers over a wide range of measurement directions. *J. Quant. Spectrosc. Radiat. Transf.* **2018**, *206*, 273–285. [CrossRef]
20. Litvinov, P.; Hasekamp, O.; Cairns, B. Models for surface reflection of radiance and polarized radiance: Comparison with airborne multi-angle photopolarimetric measurements and implications for modeling top-of-atmosphere measurement. *Remote Sens. Environ.* **2010**, *115*, 781–792. [CrossRef]
21. Su, D.; Liu, L.; Liu, L.; Ming, R.; Wu, S.; Zhang, J. An Infrared DoLP Model Considering the Radiation Coupling Effect. *Photonics* **2021**, *8*, 546. [CrossRef]
22. Stokes, G. On the comparison and resolution of streams of polarized light from different sources. *Trans. Camb. Philos. Soc.* **1852**, *9*, 399–416.
23. Talmage, D.; Curran, P. Remote sensing using partially polarized light. *Int. J. Remote Sens.* **1986**, *7*, 47–64. [CrossRef]
24. Katarina, Z.; Charles, M.; Deric, J.; Marcos, J.; Robert, A. Wavelength dependence of the bidirectional reflectance distribution function (BRDF) of beach sands. *Appl. Opt.* **2015**, *54*, F243–F255.
25. Shell, J. Polarimetric Remote Sensing in the Visible to Near Infrared. Ph.D's Thesis, Rochester Institute of Technology, Rochester, NY, USA, 2005.
26. Cook, R.; Torrance, K. A reflectance model for computer graphics. *ACM Trans. Graph.* **1981**, *1*, 7–24. [CrossRef]
27. Huang, B.; Peng, B.; Ren, Q.; Liao, S. Modeling and analysis of spectral polarization BRDF based on microfacet theory. *J. Quant. Spectrosc. Radiat. Transf.* **2024**, *313*, 108830. [CrossRef]
28. Yang, M.; Xu, W.; Sun, Z.; Jia, A.; Xiu, P.; Li, L.; Zheng, C.; Li, J. Degree of polarization modeling based on modified microfacet pBRDF model for material surface. *Opt. Commun.* **2019**, *453*, 124390. [CrossRef]
29. Blinn, J. Models of light reflection for computer synthesized pictures. *ACM SIGGRAPH Comput. Graph.* **1977**, *11*, 192–198. [CrossRef]
30. Sun, Z.; Wu, Z.; Zhao, Y. Semi-automatic laboratory goniospectrometer system for performing multi-angular reflectance and polarization measurements for natural surfaces. *Rev. Sci. Instrum.* **2014**, *85*, 014503. [CrossRef]
31. Renhorn, I.; Boreman, G. Analytical fitting model for rough-surface BRDF. *Opt. Express* **2008**, *16*, 12892–12898. [CrossRef]
32. Hyde, M.; Cain, S.; Schmidt, J.; Havrilla, M. Material classification of an unknown object using turbulence-degraded polarimetric imagery. *IEEE Trans. Geosci. Remote Sens.* **2011**, *49*, 264–276. [CrossRef]
33. Meng, L.; Kerekes, J. An analytical model for optical polarimetric imaging systems. *IEEE Trans. Geosci. Remote Sens.* **2014**, *52*, 6615–6626. [CrossRef]
34. Brown, C.E. Coefficient of variation. In *Applied Multivariate Statistics in Geohydrology and Related Sciences*; Springer: Berlin/Heidelberg, Germany, 1998; pp. 155–157.
35. Sun, Z.; Wu, D.; Lv, Y.; Zhao, Y. Polarized reflectance factors of vegetation covers from laboratory and field: A comparison with modeled results. *J. Geophys. Res. Atmos.* **2017**, *122*, 1042–1065. [CrossRef]